



**FACULTY
OF MATHEMATICS
AND PHYSICS**
Charles University

BACHELOR THESIS

Martin Vavřík

**Simulation and Reconstruction
of Charged Particle Trajectories
in an Atypic Time Projection Chamber**

Institute of Particle and Nuclear Physics

Supervisor of the bachelor thesis: Mgr. Tomáš Sýkora, Ph.D.

Study programme: Physics

Prague 2025

9 I declare that I carried out this bachelor thesis independently, and only with the
10 cited sources, literature and other professional sources. It has not been used to
11 obtain another or the same degree.

12 I understand that my work relates to the rights and obligations under the Act
13 No. 121/2000 Sb., the Copyright Act, as amended, in particular the fact that the
14 Charles University has the right to conclude a license agreement on the use of this
15 work as a school work pursuant to Section 60 subsection 1 of the Copyright Act.

In date
Author's signature

Title: Simulation and Reconstruction of Charged Particle Trajectories in an Atypical Time Projection Chamber Added hyphen to avoid overfull hbox

Author: Martin Vavřík

Institute: Institute of Particle and Nuclear Physics

Supervisor: Mgr. Tomáš Sýkora, Ph.D., Institute of Particle and Nuclear Physics

Abstract: Abstract.

Keywords: key words

Contents

| | | |
|----|--|-----------|
| 17 | | |
| 18 | Motivation | 2 |
| 19 | 0.1 ATOMKI Anomaly | 2 |
| 20 | 0.1.1 ATOMKI Measurements | 2 |
| 21 | 0.1.2 Other Experiments | 3 |
| 22 | 0.2 X17 Project at IEAP CTU | 5 |
| 23 | 1 Time Projection Chamber | 7 |
| 24 | 1.1 Orthogonal Fields TPC at IEAP CTU | 7 |
| 25 | 1.1.1 Coordinate Systems | 7 |
| 26 | 1.1.2 Magnetic Field Simulation | 8 |
| 27 | 2 Track Simulation | 11 |
| 28 | 2.1 Microscopic Simulation | 11 |
| 29 | 2.2 Runge-Kutta Simulation | 12 |
| 30 | 3 Track Reconstruction | 13 |
| 31 | 3.1 Reconstruction Assuming Steady Drift | 13 |
| 32 | 3.2 Ionization Electron Map | 15 |
| 33 | 3.2.1 Gradient Descent Search | 18 |
| 34 | 3.2.2 Interpolation on the Inverse Grid | 19 |
| 35 | 3.3 Discrete Reconstruction | 20 |
| 36 | 4 Energy Reconstruction | 22 |
| 37 | 4.1 Cubic Spline Fit | 22 |
| 38 | 4.2 Circle and Lines Fit | 24 |
| 39 | 4.2.1 Two-dimensional fit | 24 |
| 40 | 4.2.2 Three-dimensional fit | 26 |
| 41 | 4.3 Runge-Kutta Fit | 26 |
| 42 | Conclusion | 28 |
| 43 | Bibliography | 30 |
| 44 | List of Figures | 33 |
| 45 | List of Tables | 35 |
| 46 | List of Abbreviations | 36 |

Motivation

A Time Projection Chamber (TPC) is a type of gaseous detector that detects charged particle trajectories by measuring the positions and drift time of ions created in the gas; details are provided in Section 1. The energy of these particles can be inferred from the curvature of their trajectory in the magnetic field.

The goal of this thesis is to develop an algorithm for the reconstruction of charged particle trajectories and energy in an atypic TPC with orthogonal electric and magnetic fields, hereafter referred to as the Orthogonal Fields TPC (OFTPC), used in the X17 project at the Institute of Experimental and Applied Physics, Czech Technical University in Prague (IEAP CTU). Furthermore, we present the results of testing this algorithm with different samples of simulated data. (We use the Garfield++ toolkit [1] for simulations in combination with the ROOT framework [2] for data analysis and visualization. Some of our more demanding simulations are run on the MetaCentrum grid [3].)

The X17 project in IEAP CTU aims to reproduce measurements of anomalous behavior in the angular correlation distribution of pairs produced by the Internal Pair Creation (IPC) mechanism [4] during the decay of certain excited nuclei (^8Be , ^{12}C , and ^4He) observed by a team at ATOMKI in Hungary. **I would leave this here as a short summary before I explain it in more detail in the sections below.**

Add citations: X17 project, VdG. Maybe also TPC, etc.

0.1 ATOMKI Anomaly

Many theories propose the existence of new light bosons that are weakly coupled to ordinary matter [5]. These particles are potential dark matter candidates and could solve other issues with the Standard Model, such as the strong CP problem and the anomalous muon magnetic moment.

A possible way of detecting such bosons with a short lifetime is to observe nuclear transitions of excited nuclei. If a boson was emitted during the transition and subsequently decayed into an electron-positron pair, we could observe this as a peak on top of the e^+e^- angular correlation from IPC and External Pair Creation (EPC).

0.1.1 ATOMKI Measurements

Previously, there were several measurements of IPC in nuclear transitions in ^8Be at Institute für Kernphysik (Frankfurt) [6, 7, 8] and at ATOMKI [9, 10] resulting in different anomalies with invariant mass in the range 5–15 MeV. This prompted a development of a better spectrometer.

In 2015, a group at ATOMKI led by Attila Krasznahorkay observed an anomalous IPC in ^8Be [11]. They used the $^7\text{Li}(p, \gamma)^8\text{Be}$ reaction at the $E_p = 1030$ keV proton capture resonance to prepare the 18.15 MeV excited state ($J^\pi = 1^+$, $T = 0$). This state decays predominantly through M1 transitions to the ground state ($J^\pi = 0^+$, $T = 0$) and to the 3.03 MeV state ($J^\pi = 2^+$, $T = 0$) [12].

88 The angular correlation of the e^+e^- pairs created internally in these transitions
 89 were measured and compared to the simulation; results from a narrow $E_{\text{sum}} =$
 90 $= 18$ MeV region are shown in Figure 1a. The simulation includes boson decay
 91 pairs for different boson masses. The disparity parameter y is defined as

$$y = \frac{E_{e^-} - E_{e^+}}{E_{e^-} + E_{e^+}}, \quad (1)$$

92 where E_{e^-} and E_{e^+} are the kinetic energies of the electron and positron.

93 Their experimental setup was later upgraded ([details?](#)) and used for new mea-
 94 surements. In 2022 the ^8Be anomaly was also measured using the $E_p = 441$ keV
 95 resonance to produce the 17.64 MeV excited state ($J^\pi = 1^+$, $T = 1$) which again
 96 decays primarily to the ground state and the 3.03 MeV state [12]. The anomaly
 97 was also measured for $E_p = 650$ and 800 keV where E1 transitions from the direct
 98 proton capture dominate [13]. The results for e^+e^- with $E_{\text{sum}} \in [13.5, 20]$ MeV
 99 are shown in Figure 1b.

100 The newer setup was also used in 2021 to study the $^3\text{H}(p, e^+e^-)^4\text{He}$ reaction at
 101 $E_p = 510, 610$ and 900 keV [14], inducing direct and resonant capture populating
 102 the overlapping first 20.21 MeV ($J^\pi = 0^+$) and second 21.01 MeV ($J^\pi = 0^-$)
 103 excited states [15]. The comparison of simulated and measured e^+e^- pair angular
 104 correlations in the $E_{\text{sum}} \in [18, 22]$ MeV region is shown in Figure 1c.

105 In 2022, another anomaly was measured in the $^{11}\text{B}(p, e^+e^-)^{12}\text{C}$ process [16].
 106 The $E_p = 1388$ keV resonance was used to populate the 17.23 MeV excited state
 107 ($J^\pi = 1^-$, $T = 1$) with a large width $\Gamma = 1.15$ MeV [17]. This state decays
 108 mainly through E1 transitions to the ground state $J^\pi = 0^+$ and to the 4.44 MeV
 109 state $J^\pi = 2^+$. To compensate for energy losses in the target, five energies in
 110 the range $E_p = 1.5\text{--}2.5$ MeV were used. The experimental angular correlation for
 111 the 17.23 MeV transition to the ground state is shown in Figure 1d.

112 Possible explanations of the anomaly include experimental effects, higher or-
 113 der processes in the Standard Model [18, 19] or even a protophobic fifth force
 114 mediated by a new 17 MeV boson X17 [20].

115 0.1.2 Other Experiments

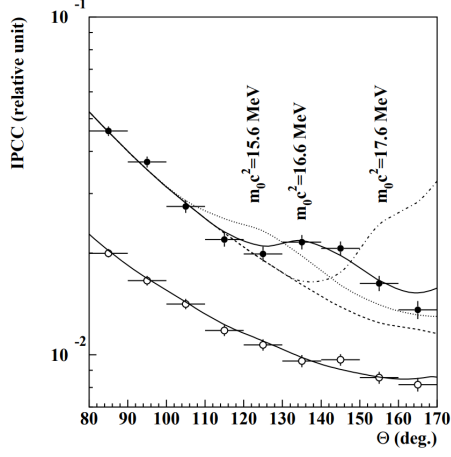
116 Since the ATOMKI measurements, several experiments have been initiated to
 117 attempt to replicate the results and search for the hypothetical X17 particle.

118 Two-arm e^+e^- spectrometer in Hanoi

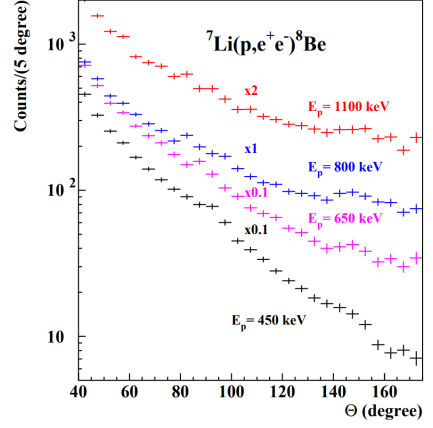
119 The anomaly in ^8Be has been observed with $> 4\sigma$ confidence by a team at the
 120 Hanoi University of Sciences for $E_p = 1225$ keV [21]. They built a two-arm
 121 spectrometer in collaboration with ATOMKI and calibrated it using the 17.6 MeV
 122 M1 transition. The results are shown in Figure 2.

123 Collisions at Nuclotron in Dubna

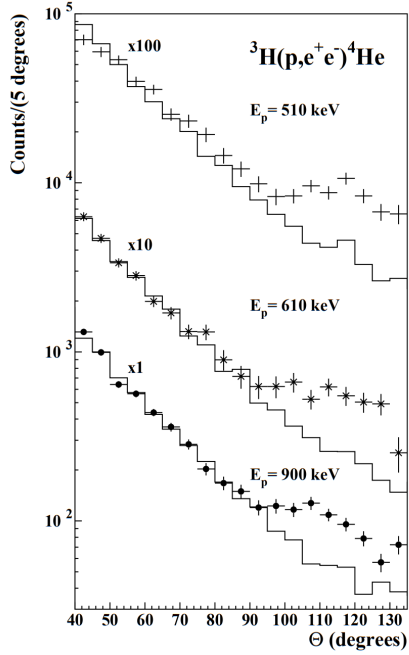
124 At the Joint Institute for Nuclear Research in Dubna, signal in the form of en-
 125 hanced structures in the $\gamma\gamma$ spectra at ~ 17 and ~ 38 MeV invariant masses
 126 for $p + \text{C}$, $d + \text{C}$ and $d + \text{Cu}$ reactions at momenta 5.5, 2.75, and 3.83 GeV per
 127 nucleon [22]. Monte Carlo simulations support the conclusion that the signals
 128 are a consequence of a decay of unknown particles X17 and E38.



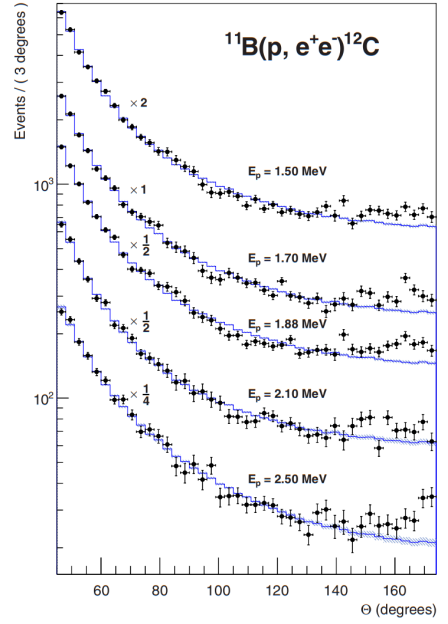
(a) Experimental e^+e^- pair correlations measured in the ${}^7\text{Li}(p, e^+e^-){}^8\text{Be}$ reaction with $|y| \leq 0.5$ (closed circles) and $|y| \geq 0.5$ (open circles) [11].



(b) Experimental e^+e^- pair correlations measured in the ${}^7\text{Li}(p, e^+e^-){}^8\text{Be}$ reaction with the improved setup for different proton beam energies [13].



(c) Experimental e^+e^- pair correlations measured in the ${}^3\text{H}(p, e^+e^-){}^4\text{He}$ reaction with $|y| \leq 0.3$ for different proton beam energies [14].



(d) Experimental e^+e^- pair correlations measured in the ${}^{11}\text{B}(p, e^+e^-){}^{12}\text{C}$ reaction for different proton beam energies [16].

Figure 1: The ATOMKI anomalous IPC measured for different nuclei.

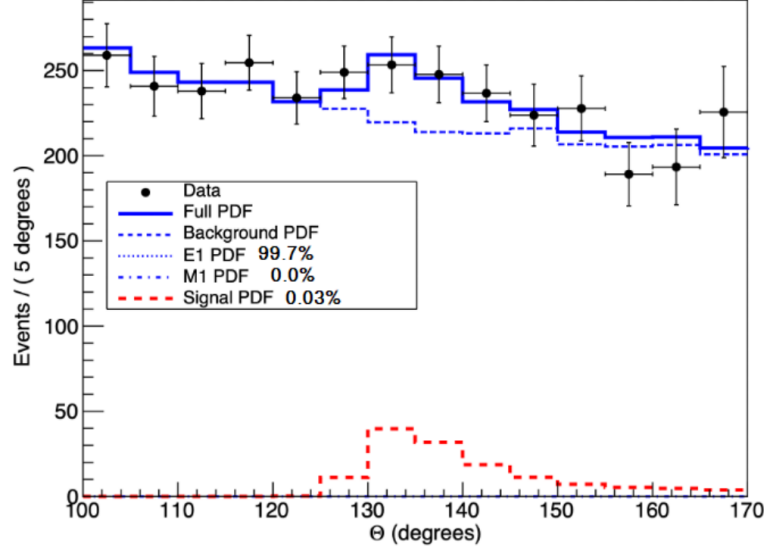


Figure 2: Results from the Hanoi spectrometer – angular e^+e^- pair correlations measured in the ${}^7\text{Li}(p, e^+e^-){}^8\text{Be}$ reaction at $E_p = 1225$ keV [21].

129 The MEG II (Muon Electron Gamma) experiment

130 Experiments using the ${}^7\text{Li}(p, e^+e^-){}^8\text{Be}$ reaction were carried out at the Paul
 131 Scherrer Institute with the MEG II superconducting solenoid spectrometer [23].
 132 Analysis of the data with $E_p = 1080$ keV exciting both of the resonances (beam
 133 fully stopping in the target) found no significant evidence supporting the X17
 134 hypothesis, results are shown in Figure 3. An upper bound (at 90% confidence)
 135 on the X17-to- γ branching ratio was set at $1.2 \cdot 10^{-5}$ for the 18.15 MeV state
 136 (larger than the ratio $5.8 \cdot 10^{-6}$ obtained by ATOMKI in 2016). **Could add their**
 137 **90% C.L bounds figure also.**

138 0.2 X17 Project at IEAP CTU

139 The aim of the X17 project at the Van der Graaff facility of the Institute of
 140 Experimental and Applied Physics, Czech Technical University in Prague is to
 141 repeat the original ATOMKI experiments with ${}^7\text{Li}$ and ${}^3\text{H}$ targets using an inde-
 142 pendent e^+e^- spectrometer. In order to effectively measure the anomaly, we need
 143 to reconstruct both the energy and the angular correlation of the e^+e^- pairs. The
 144 spectrometer will use three layers of detectors to achieve this – Timepix 3 (Tpx3)
 145 silicon pixel detector and Multi-Wire Proportional Chamber (MWPC) layers for
 146 the angle reconstruction and a Time Projection Chamber (TPC) layer for the en-
 147 ergy reconstruction. **Spectrometer CAD drawing (coordinates here or next chap-**
 148 **ter?). Cite some VdG paper, mention grant? Using [https://cernbox.cern.ch/](https://cernbox.cern.ch/pdf-viewer/public/rf0oU1nqVLN3acZ/LuzH_submitted.pdf)**
 149 **[pdf-viewer/public/rf0oU1nqVLN3acZ/LuzH_submitted.pdf](https://cernbox.cern.ch/pdf-viewer/public/rf0oU1nqVLN3acZ/LuzH_submitted.pdf).**

150 The energy of e^+e^- pair produced in the reaction is given by the energy
 151 available E_r in the reaction and can be distributed between them arbitrarily.
 152 Nonetheless in the decay of the hypothetical X17 particle, electron and positron
 153 should have similar energy and we can therefore use a disparity cut $|y| \leq 0.5$ for
 154 the disparity parameter (defined in Equation 1). Interesting events should rarely

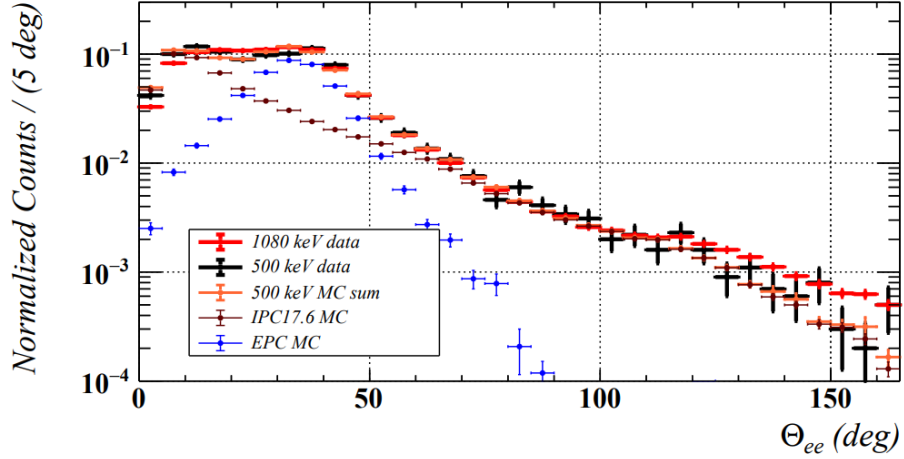


Figure 3: Results from the MEG II experiments – angular correlation of e^+e^- pairs with $E_{\text{sum}} \in [16, 20]$ MeV measured in the ${}^7\text{Li}(p, e^+e^-){}^8\text{Be}$ reaction with proton beam energies 500 and 1080 keV. The 500 keV dataset is fitted with Monte Carlo of both the IPC deexcitation and the EPC produced by gammas [23].

155 have a particle with an energy below $E_r/4$ (roughly 4 MeV). Electrons with such
 156 low energies are scattered significantly by even a thin layer of relatively light
 157 material, for this reason the Tpx3 layer will be inside of the vacuum tube and the
 158 tube will have a thinned aluminum segment or KaptonTM windows.

159 Tpx3 can measure (in each $55 \times 55 \mu\text{m}$ pixel) time-of-arrival (ToA) with 1.6 ns
 160 precision and time-over-threshold (ToT) which reflects the deposited energy. This
 161 potentially allows 3D tracking if we increase the chip thickness at the cost of in-
 162 creased scattering. The layer can reconstruct the reaction vertex and the angular
 163 correlation with high precision.

164 The layer of MWPCs with sensitive area $40 \times 38 \text{ mm}^2$ will be outside of
 165 the beam pipe. It will provide an extra point on the particle trajectory which can
 166 help with the estimation of the reaction vertex and improve the TPC performance
 167 by providing its entry point.

168 The TPCs, which are a subject of this theses, are in a magnetic field of per-
 169 manent magnets positioned between them and provide 3D track reconstruction
 170 and subsequent momentum and particle identification (its charge, or even type
 171 based on its stopping power). They avoid radiative losses thanks to the small
 172 interaction with the incident particle. For the readout, triple Gas Electron Mul-
 173 tiplier (GEM) will be used. The magnetic field layout in our TPCs is atypical –
 174 orthogonal to the electric field inside the chamber, this is why we call them Or-
 175 thogonal Fields TPC (OFTPC). Further details about our OFTPCs are provided
 176 in section 1.1.

1. Time Projection Chamber

Description of TPC, working principle, standard vs. our field layout.

1.1 Orthogonal Fields TPC at IEAP CTU

Short description of our detector. Why we use an atypic TPC (benefits, complications). Gas mixture used in the detector (70/30) and its effect.

1.1.1 Coordinate Systems

In order to describe events in our detector, we use three distinct spaces: the detector space \mathcal{D} , the readout space \mathcal{R} and the pad space \mathcal{P} . Each space is later used to represent ionization electrons at different stages of the detection process: their creation in the gas, their final position when hitting the readout plane, and finally their representation in the discrete pad space.

Detector Space

The detector space \mathcal{D} represents the physical space of our detector. We describe it using Cartesian coordinates (x, y, z) . The z -axis is the detector's axis of symmetry, with its negative direction aligned with the proton beam. The origin $(0, 0, 0)$ is located at the center of the irradiated target. The positive x -axis passes through the center of one of the OFTPCs along the intersection of its two planes of symmetry. The y -axis is then chosen to maintain a right-handed coordinate system.

Since the detector has a hexagonal symmetry, we use only one of its sectors in this work – the first sector $\mathcal{D}_1 \subset \mathcal{D}$ which is defined by the condition:

$$(x, y, z) \in \mathcal{D}_1 \Leftrightarrow |y| \leq x \tan \frac{\pi}{6}. \quad (1.1)$$

Simulations in this sector can be applied to all sectors by rotating the coordinates accordingly. The volume of the OFTPC in this sector, which has the shape of a trapezoidal prism, has these boundaries:

$$x \in [x_{\min}, x_{\max}] = [6.51, 14.61] \text{ cm}, \quad (1.2)$$

$$z \in [z_{\min}, z_{\max}] = [-8, 8] \text{ cm}, \quad (1.3)$$

$$y_{\max}(x_{\min}) = -y_{\min}(x_{\min}) = 2.75 \text{ cm}, \quad (1.4)$$

$$y_{\max}(x_{\max}) = -y_{\min}(x_{\max}) = 7.45 \text{ cm}, \quad (1.5)$$

where $y_{\max}(x)$ is the maximal value of the y -coordinate for a given x . The readout is located at $z = 8 \text{ cm}$; for some purposes, we also define the distance to the readout $d_r = 8 \text{ cm} - z$ as an alternative to the z -coordinate. Keeping this paragraph as it is because the OFTPC volume is distinct from the first sector and some parts of this thesis use the space beyond this volume.

206 Readout Space

207 The readout space \mathcal{R} represents the drift time and final positions of ionization
 208 electrons as measured by an ideal continuous readout. We describe it using
 209 coordinates (x', y', t) , where x' and y' correspond to the detector coordinates at
 210 the readout plane ($z = 8$ cm). **Currently not entirely sure how to put this into**
 211 **a figure since only x' and y' correspond to the detector coordinates. The drift**
 212 **time t is approximately proportional to d_r .**

213 Pad Space

214 The pad space \mathcal{P} represents the time bin and pad number of ionization electrons
 215 as measured by an ideal discrete readout. **It is not really a subspace of \mathcal{R} but**
 216 **there is a mapping from \mathcal{R} to \mathcal{P} . It is a discretization of a part of \mathcal{R} , the mapping**
 217 **can be adjusted depending on the simulation. If we assume uniform electric field**
 218 **there will be gaps, we don't use gaps in the reconstruction since the electrons**
 219 **should be pulled towards the pads.**

220 The readout of the OFTPC will consist (**is the design final?**) of 128 rectangular
 221 pads arranged in a staggered pattern (**add image where all the parameters are**
 222 **marked**). Most of the pads are 0.6×0.9 cm, only pads 102 and 124 are 0.6×0.6 cm,
 223 pad 127 is 0.6×0.509 cm. The distance of neighboring pads is 0.08 cm, staggering
 224 offset is 0.3946 cm.

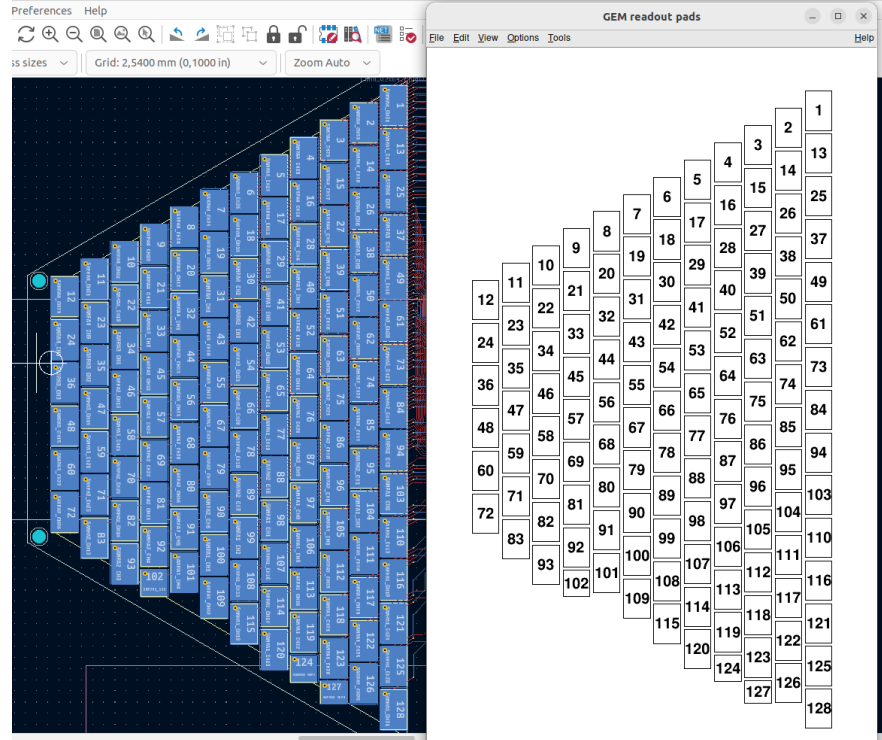


Figure 1.1: Pad layout of the TPC. **Swap for better image.**

225 1.1.2 Magnetic Field Simulation

226 **Magnetic field simulations in Maxwell (citation). Some figures. When working**
 227 **with the magnetic field outside the regular grid, we use trilinear interpolation.**

228 Trilinear Interpolation

229 Trilinear interpolation is a 3D generalization of linear interpolation. It can be
 230 used to interpolate a function whose values are known on a regular grid with
 231 rectangular prism cells. We use this simple method for interpolating the magnetic
 232 field, and it is later used in Section 3.2.1 to interpolate the Ionization Electron
 233 Map, a key component of our track reconstruction algorithm. In both cases, we
 234 use a regular cubic grid (apparently it is also called a Cartesian grid).

235 Could put a paragraph about linear interpolation here if it is not clear from
 236 the equations below.

237 Let us consider a cell of our regular grid (a cube) with an edge of length a
 238 containing the point $\mathbf{C} = (x, y, z)$ where we want to interpolate a function
 239 $f: \mathbb{R}^3 \rightarrow \mathbb{R}$. We know the values of this function at the vertices of the cell
 240 $\mathbf{C}_{ijk} = (x_0 + ia, y_0 + ja, z_0 + ka)$, where $i, j, k \in \{0, 1\}$ are indices. We also define
 241 the points $\mathbf{C}_{ij} = (x, y_0 + ia, z_0 + ja)$ and $\mathbf{C}_i = (x, y, z_0 + ia)$. Then the interpolated
 242 value $\hat{f}(\mathbf{C})$ can be calculated as a composition of three linear interpolations (see
 243 Figure 1.2):

$$\hat{f}(\mathbf{C}_{ij}) = (1 - x_d) f(\mathbf{C}_{0ij}) + x_d f(\mathbf{C}_{1ij}), \quad (1.6)$$

$$\hat{f}(\mathbf{C}_i) = (1 - y_d) \hat{f}(\mathbf{C}_{0i}) + y_d \hat{f}(\mathbf{C}_{1i}), \quad (1.7)$$

$$\hat{f}(\mathbf{C}) = (1 - z_d) \hat{f}(\mathbf{C}_0) + z_d \hat{f}(\mathbf{C}_1), \quad (1.8)$$

244 where x_d, y_d , and z_d are given as follows:

$$x_d = \frac{x - x_0}{a}, \quad y_d = \frac{y - y_0}{a}, \quad z_d = \frac{z - z_0}{a}. \quad (1.9)$$

245 We can also write

$$\hat{f}(\mathbf{C}) = \sum_{i,j,k \in \{0,1\}} t_x^i t_y^j t_z^k f(\mathbf{C}_{ijk}), \quad (1.10)$$

$$t_\alpha \stackrel{\text{def}}{=} \begin{pmatrix} t_\alpha^0 \\ t_\alpha^1 \end{pmatrix} = \begin{pmatrix} 1 - \alpha_d \\ \alpha_d \end{pmatrix}, \quad (1.11)$$

246 where $\alpha \in \{x, y, z\}$ is an index. Furthermore, we can write $\hat{f}(\mathbf{C})$ as a polynomial:

$$\hat{f}(\mathbf{C}) = \sum_{\alpha, \beta, \gamma \in \{0,1\}} \sum_{i=0}^{\alpha} \sum_{j=0}^{\beta} \sum_{k=0}^{\gamma} (-1)^{(\alpha-i)+(\beta-j)+(\gamma-k)} f(\mathbf{C}_{ijk}) x_d^\alpha y_d^\beta z_d^\gamma. \quad (1.12)$$

247 We take advantage of this form when generalizing trilinear interpolation to irreg-
 248 ular grid in section 3.2.2.

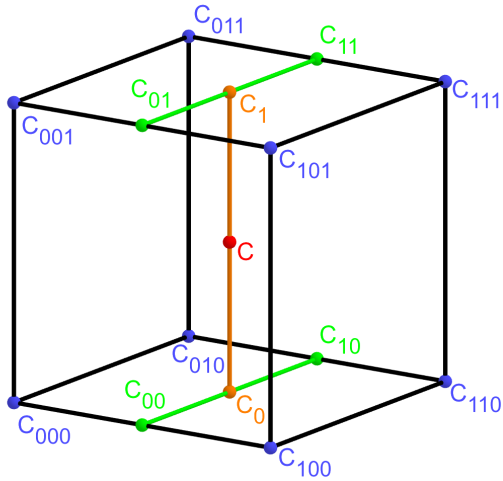


Figure 1.2: Visualization of trilinear interpolation as a composition of linear interpolations. Image drawn in GeoGebra and inspired by a similar image on Wikipedia (which looks a bit worse) – is credit necessary?

249 Maybe a citation here, although I am not sure it is necessary since it could
 250 be considered common knowledge. The last two equations are my own. Maybe
 251 x_0 , etc. should be explicitly described.

2. Track Simulation

In order to develop and test the reconstruction algorithm, electron and positron tracks are simulated inside the first sector \mathcal{D}_1 of our detector (see Section 1.1.1) with different initial parameters. Two approaches are currently used to simulate tracks, each of them for different purpose.

The **Microscopic Simulation** uses the Garfield++ toolkit [1]. Within this toolkit, the High Energy Electro-Dynamics (HEED) program [24] is used to simulate the primary particle and the class *AvalancheMicroscopic* to simulate the drift of secondary electrons created by ionization in the gas. This is the most precise and time-consuming simulation used; our current goal is to be able to successfully reconstruct its results and determine our best-case energy resolution.

The **Runge-Kutta Simulation** uses the 4th order Runge-Kutta numerical integration (add citation for Runge-Kutta) to simulate the trajectory of the primary particle in the electromagnetic field inside the detector. It is relatively fast since it does not simulate the secondary particles. It is used as part of our reconstruction algorithm and for testing some parts of the reconstruction.

All of these simulations require the knowledge of the electromagnetic field inside the detector. A uniform electric field of $400 \text{ V}\cdot\text{cm}^{-1}$ is assumed. The magnetic field was simulated in Maxwell (see Section 1.1.2). add citation

Single track in positive x direction or initial parameter randomization. Importance of gas composition, used gas compositions.

2.1 Microscopic Simulation

The microscopic simulation, the most detailed simulation used in this work, is performed using the Garfield++ toolkit [1].

The electron transport properties are simulated using the program Magboltz (Add citation.). Two different gas mixtures were used: 90% Ar + 10% CO₂ and 70% Ar + 30% CO₂. The second mixture will be used in our detector. The temperature is set to 20 °C, the pressure is atmospheric.

The primary track is simulated using the program HEED [24], which is an implementation of the photo-absorption ionization model. This program provides the parameters of ionizing collisions. HEED can also be used to simulate the transport of delta electrons; we do not account for these in the current simulation but plan to include them in the future. The photons created in the atomic relaxation cascade (fluorescence reabsorption, ?) are also not simulated.

Finally, we use the microscopic tracking provided by the class *AvalancheMicroscopic* to simulate the drift of the ionization electrons. Each electron is followed from collision to collision using the equation of motion and the collision rates calculated by Magboltz.

First simulated track in the z direction should be described in detail here (own subsection?). Figures.

Add more detailed and better description of HEED, and microscopic tracking (each their own subsection?). Could also mention Monte Carlo (requires gas file generation) and Runge-Kutta simulation implemented in Garfield, why we don't

295 use them (another subsection? rename the section to Garfield++ simulation and
 296 mention all relevant parts?).

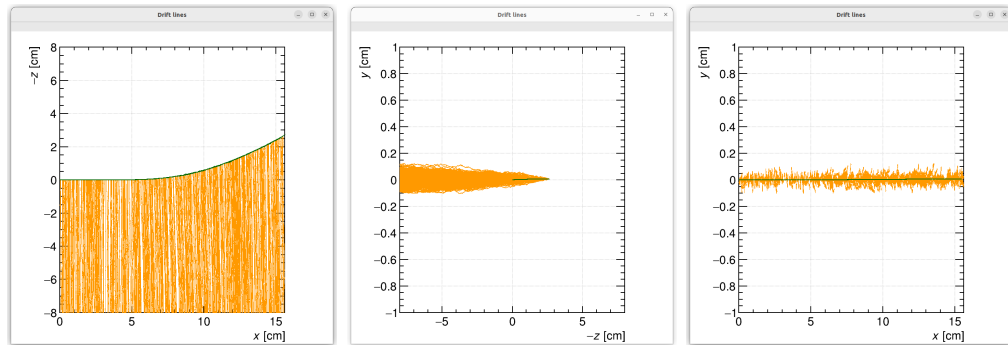


Figure 2.1: Example of a simulated electron track in 70 % argon and 30 % CO₂ atmosphere (on the left). Swap for better images, better zoom. Explain drift lines, primary particle.

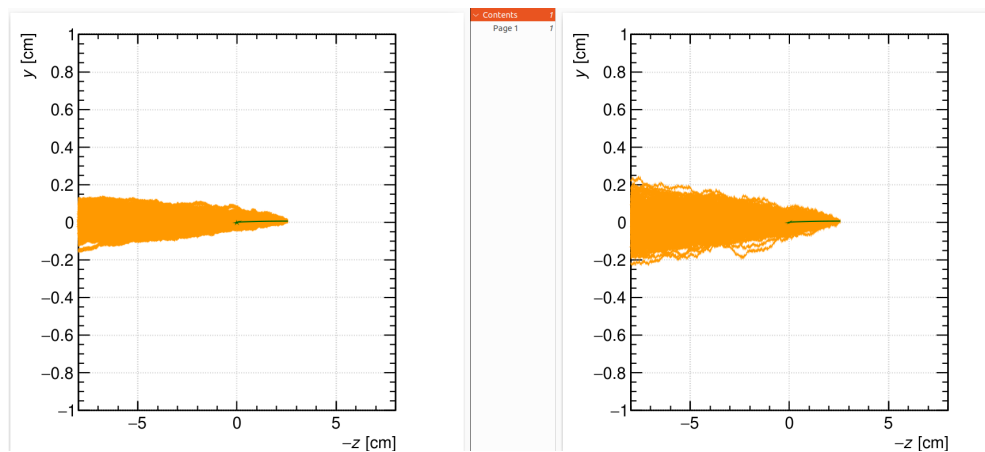


Figure 2.2: Comparison of diffusion in a simulated electron track in 70 % argon, 30 % CO₂ atmosphere and in 90 % argon, 10 % CO₂ atmosphere (on the right). Swap for better image, better zoom. Or put the same pictures for both comparisons in one subfigure, etc. Describe better.

297 2.2 Runge-Kutta Simulation

298 Trajectory simulation with 4th order Runge-Kutta. Relativistic equation that is
 299 numerically integrated by the algorithm.

3. Track Reconstruction

In the first stage of the reconstruction algorithm, we reconstruct the track of a primary particle (either an electron or a positron). The result of this step is then used to determine the energy of the particle (Section 4).

The **Reconstruction Assuming Steady Drift** uses the standard TPC approach. With parallel fields, the drift inside a uniform electric field remains undistorted (reference to some future part of the TPC chapter). Therefore, we only need to reconstruct the z -coordinate from the drift time using the known drift velocity. We also assume that the readout coordinates (x', y', t) are known exactly, neglecting the pads and time bins.

Reconstruction using the **Ionization Electron Map** (from now on referred to as *the map*) uses a simulation of the drift of secondary (ionization) electrons within the detector volume. This simulation can then be used to interpolate the initial position of the secondary electrons. First attempts neglect the pads.

We use the map for reconstruction in two different ways. The first one uses gradient descent search along with trilinear interpolation (see Section 1.1.2) of the map. The second method uses interpolation on the irregular inverse grid with a linear polynomial.

The **Discrete Reconstruction** uses the map; instead of reconstructing the exact position of each electron, we reconstruct the center of each hit pad with the time corresponding to the midpoint of the time bin. The electron count in each TPC bin (consisting of the pad and the time bin) serves as the charge value, which is then used as a weight in the energy reconstruction fit.

3.1 Reconstruction Assuming Steady Drift

As the first step, we decided to try to reconstruct an electron track with a special set of initial parameters. The origin of the particle is given by the origin of our coordinate system. The initial direction is given by the positive x -axis. This means the magnetic field of our detector is perpendicular to the momentum of the particle at all times, and we can reduce the problem to two-dimensional space. As an example, we use a track simulated using the microscopic simulation (see Section 2.1) with a kinetic energy of 8 MeV. The gas composition used in this simulation is 90% Ar + 10% CO₂. Might be better to describe this track in Section 2.1.

In this approach to the reconstruction of the track, we decided to use the common method used in a standard TPC. This will allow us to explore the significance of the atypical behavior in our OFTPC. Additionally, we assume the readout is continuous to further simplify the problem. In this approximation, we reconstruct the initial position of each ionization electron.

The reconstruction is then defined by the following relations between the coordinates of the detector space and the readout space (see Section 1.1.1):

$$x = x', \tag{3.1}$$

$$y = y', \tag{3.2}$$

$$z = v_d t, \tag{3.3}$$

where v_d is the drift velocity of electrons in the given gas mixture. At a phenomenological level, this velocity can be considered as a function of the electric field \mathbf{E} and the magnetic field \mathbf{B} :

$$v_d = v_d(\mathbf{E}, \mathbf{B}). \quad (3.4)$$

Equation taken from Garfield user manual. The Garfield++ toolkit uses this fact to accelerate their drift simulation with non-microscopic approaches (could mention in the simulation chapter). Since we assume a uniform electric field in our detector and we want to neglect the effect of our unusual magnetic field, we consider the drift velocity to be constant in this scenario. We then approximate this velocity by fitting the dependence $z(t)$ taken from the simulated ionization electrons. This is in one of the provisional figures. Also, this description is not completely accurate; in reality, we fit $t1:8-y0$ with $a1*x+a0$ and then invert this and use $8-y0 = b1*t1+b0$ (old coordinates); $b1=1/a1$ functions as the drift velocity. Maybe also define this 8-z variable as an alternative to z in Section 1.1.1 and then use it when correcting this.

Later, in a commit after this, I plotted some residues (provisional figure), which could be useful, but for some reason they are residuals from a spline fit of the track?! Probably redo this without the spline fit; just explore the difference in individual points.

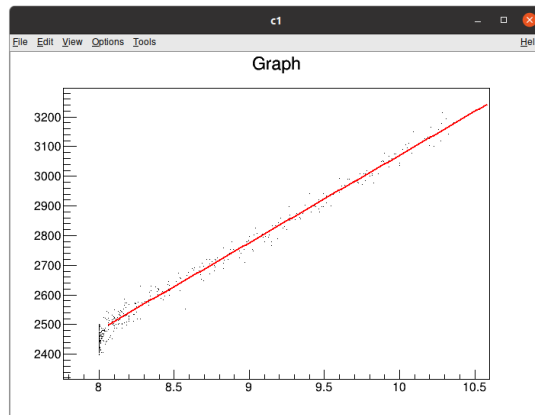


Figure 3.1: Dependence of the drift time on the z coordinate in 90 % argon and 10 % CO_2 atmosphere, fitted with a linear function. The fitted function gives us the average drift velocity in the gas and can be used for rough reconstruction in our TPC. Swap for better image with axis labels, etc. Maybe write the fitted equation.

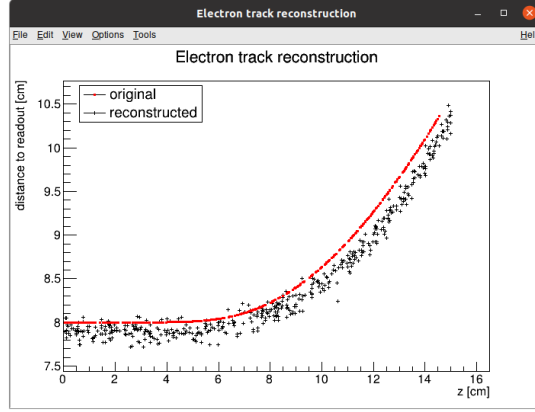


Figure 3.2: First attempt at a track reconstruction using only the drift velocity. This approach works well in a standard TPC (ideally cite some source?). 90 % argon and 10 % CO₂ atmosphere. Swap for better image, correct coordinates.

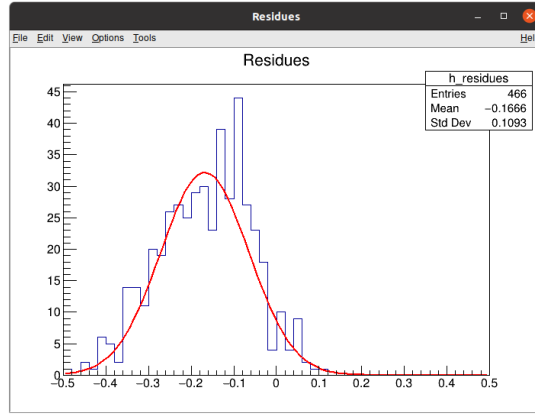


Figure 3.3: First attempt at a track reconstruction using only the drift velocity, residues. Swap for better image, correct coordinates. What's causing the shift? Explain details.

3.2 Ionization Electron Map

Inside an OFTPC, the drift of the secondary (ionization) electrons is significantly affected by its magnetic field (pictures of the distortion later, the effect is bigger for the 90/10 composition.). We need to take this into account for accurate reconstruction. In the first approximation, we assume a continuous readout (i.e., we neglect pads). We can then reconstruct the original position of each ionization electron using its readout coordinates. For this purpose, we use the ionization electron map.

The ionization electron map represents a mapping from the detector space to the readout space (see Section 1.1.1). It tells us what readout coordinates (x', y', t) we can expect on average for an ionization electron created at the detector coordinates (x, y, z) . More precisely it is a mapping to the distributions on the readout space; we can simplify this as only the means $\bar{\mathcal{M}}$ and the covariance

371 matrices \mathcal{M}_{cov} , assuming Gaussian distribution.

$$\mathcal{M} : \mathcal{D} \longrightarrow \mathcal{R}, (x, y, z) \longmapsto (x', y', t). \quad (3.5)$$

372 To get an approximation of this mapping, we simulate the drift of ionization
 373 electrons generated on a regular grid inside the volume of our OFTPC ¹. It
 374 is also useful to simulate multiple (100 in our case) electrons originating from
 375 the same position so we can get a better information about the average drift
 376 and its variance. In order to get more accurate results, we use the microscopic
 377 simulation of these electrons described in Section 2.1. When evaluating the map
 378 inside the grid, we use trilinear interpolation (see Section 1.1.2). From now on,
 379 we will denote this interpolated simulation with the same symbol \mathcal{M} .

380 Finally, we need to invert the map to get the original detector coordinates
 381 (x, y, z) for the given readout coordinates (x', y', t) . In our case, we can reason-
 382 ably assume that the mapping $\overline{\mathcal{M}}$ is one-to-one (as seen in the simulations). We
 383 implemented two methods for this purpose: the gradient descent search (Sec-
 384 tion 3.2.1) and interpolation on the inverse grid (Section 3.2.2).

385 The simulation of the map is a computationally heavy task. For this reason,
 386 we use the MetaCentrum grid [3] to parallelize needed calculations. At first, this
 387 was done by evenly distributing the simulated electrons across the individual jobs
 388 in a simulation with only one electron per vertex in the regular grid with a spacing
 389 of one centimeter.

390 Later, a more efficient approach was implemented, accounting for the varying
 391 lengths of the drift of individual electrons. If we index the electrons in the order
 392 of increasing coordinates y, x, z (picture?), we can express the number n_l of full
 393 XY layers (i.e., electrons with the same z coordinate) of electrons with index less
 394 than or equal to i

$$n_l(i) = \left\lfloor \frac{i}{n_{xy}} \right\rfloor, \quad (3.6)$$

395 where n_{xy} is the number of electrons in each XY layer calculated simply by count-
 396 ing the electrons that satisfy boundary conditions for x and y . These conditions
 397 should be mentioned above; sector condition + maximal x value. The number of
 398 electrons remaining in the top layer is then

$$n_r(i) = i \bmod n_{xy}. \quad (3.7)$$

399 Finally, we can calculate the sum of the drift gaps of electrons up to index i

$$d_{\text{sum}} = (z_{\text{max}} - z_{\text{min}})n_{xy}n_l - \frac{n_l(n_l - 1)}{2}n_{xy}l + n_r(z_{\text{max}} - z_{\text{min}} - n_l l). \quad (3.8)$$

400 We then use a binary search algorithm to find the maximum index i such that
 401 the value of this sum is less than the fraction $\frac{\text{job id}}{\text{max job id}}$ of the total sum. This way
 402 we obtain the minimal and the maximal index of electrons simulated in the given
 403 job. The spacing l should be probably defined above + picture of the simulating
 404 grid (1 layer). zmin zmax also

405 After the simulation of the map, we calculate the mean readout coordinates
 406 assuming Gaussian distribution (i.e., we use averages). We also calculate standard

¹we do not take the detector walls into account and simulate even outside of the OFTPC which lets us interpolate even close to the walls

407 deviations in a later commit, should be upgraded to the covariance matrix. We
 408 never actually plotted the distributions we get when simulating the same electron
 409 multiple times, so we do not know if our assumptions are accurate (could also
 410 run some statistical test to see how well the Gaussian distribution fits).

411 The obtained map is then stored in a custom class template *Field*, could
 412 expand on that. Maybe earlier, since the same template is used for the magnetic
 413 field.

414 Could insert a table here describing all 4 simulations of the map (gas composi-
 415 tion, spacing, etc.). Simulation inside of one sector (at first double angle). Extra
 416 space on the sensor. Edge cases not taken into account (TPC wall). Using qsub
 417 (not sure if important). Add plots of distortion of the coordinates. Could also do
 418 these plots in a different way (e.g., drawing all the endpoints of each ionization
 419 electron or some error ellipse plot).

420 Images to add (comparison of both simulations):

- 421 • 3D visualization of the map, simulation example
- 422 • z vs. t plot
- 423 • XY plane distortion for different z values; with arrows and error bars, for
 424 all z -layers with different colors
- 425 • XZ plane ($y = 0$) distortion in x (maybe not necessary?)
- 426 • XT plot ($y = 0$) showing (small) distortion in drift times

427 More images:

- 428 • Residuals of the continuous readout reconstruction.

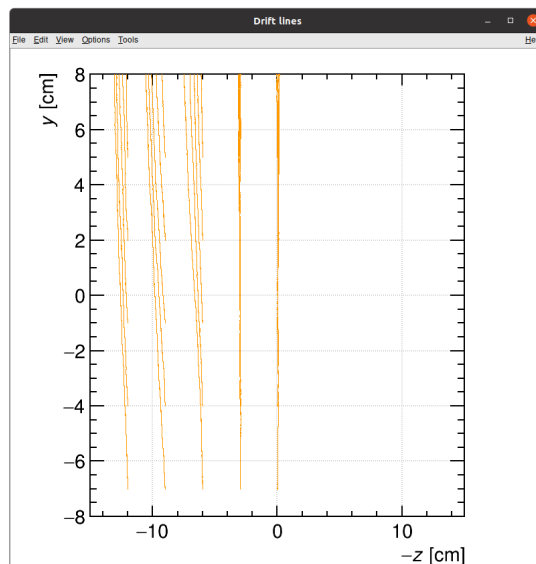


Figure 3.4: Example of map generation. Swap for better image, correct coordinates.

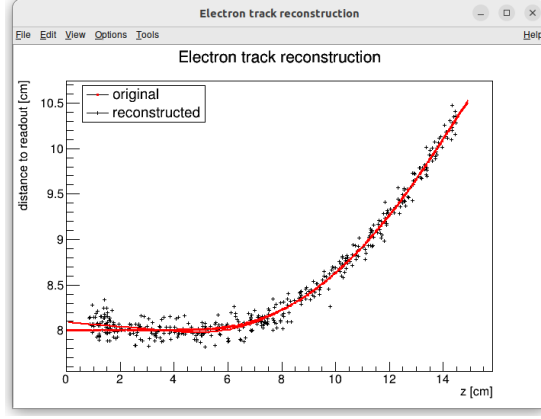


Figure 3.5: Example reconstruction with the map. Swap for better image, correct coordinates.

3.2.1 Gradient Descent Search

The first implemented method of reconstruction uses a gradient descent search to calculate an inversion of the map $\bar{\mathcal{M}}$ in a given point. Gradient descent is an iterative minimization algorithm for multivariate functions. Let $R \in \mathcal{R}$ be a point in the readout space; we want to find a point $D = (x, y, z) \in \mathcal{D}$ in the detector space such that

$$\bar{\mathcal{M}}(D) = R = (x'_R, y'_R, t_R). \quad (3.9)$$

We define a function f_R in the readout space as a distance in this space:

$$f_R(x', y', t) = \sqrt{(x' - x'_R)^2 + (y' - y'_R)^2 + v_d^2(t - t_R)^2}, \quad (3.10)$$

where v_d is an approximation of the drift velocity in the TPC, obtained from the reconstruction in Section 3.1 (there will be an image with the linear fit there). We make an initial guess (actually in the original code we just take $z = 0$):

$$D_0 = (x'_R, y'_R, v_d t). \quad (3.11)$$

Assuming we have the n -th estimate D_n , we calculate the i -th component of the gradient of $f_R \circ \bar{\mathcal{M}}$ numerically using central differences:

$$\left[\nabla(f_R \circ \bar{\mathcal{M}}) \right]^i(D_n) \approx \frac{f_R(\bar{\mathcal{M}}(D_n + s \cdot e^i)) - f_R(\bar{\mathcal{M}}(D_n - s \cdot e^i))}{2s}, \quad (3.12)$$

where $e^i \in \mathcal{D}$ is the i -th coordinate vector and s is the step size. The step size should be sufficiently small; initially, we set it as a fraction of the map's grid spacing $s = \frac{l}{10}$. During the minimization, we check that $f_R(\bar{\mathcal{M}}(D_n)) < 10s$ at all times. When using trilinear interpolation, it would be more efficient to calculate the gradient explicitly (\pm same result). This could be implemented inside the *Field* template class. The next iteration can be calculated as follows:

$$D_{n+1} = D_n - \gamma \nabla(f_R \circ \bar{\mathcal{M}})(D_n), \quad (3.13)$$

where $\gamma \in \mathbb{R}^+$ is the damping coefficient. It should be set to a small enough value to ensure convergence, but large enough for sufficient converging speed.

449 The minimization stops either when the error $f_R(\overline{\mathcal{M}}(D_n))$ drops below a specified
 450 value or when the number of iterations exceeds a certain limit (in this case,
 451 a message is printed into the console). The parameters of this method can be
 452 further optimized (e.g., a better choice of γ , **gradient computation**); instead, we
 453 later decided to use the interpolation on the inverse grid described in the next
 454 section.

455 **Measure reconstruction duration and compare it with the inverse grid inter-**
 456 **polation? Also compare the result? Not sure if this has to be cited.**

457 3.2.2 Interpolation on the Inverse Grid

458 **Interpolating between known points in the readout space. Gaussian elimina-**
 459 **tion, multivariate polynomial. Benefits compared to the gradient descent search**
 460 **method (one-time computation for the whole map is easy to achieve if needed).**

461 The currently used baseline reconstruction method is the interpolation on
 462 the inverse grid. Rather than attempting to invert the trilinearly interpolated
 463 map as in the previous section, we take advantage of the fact that the map $\overline{\mathcal{M}}$
 464 is one-to-one (**isomorphism is supposed to preserve structure, not sure how to**
 465 **interpret that here**). Since we have simulated values of this map on a regular
 466 grid in the detector space \mathcal{D} , we also know the inverse map $\overline{\mathcal{M}}^{-1}$ on the irregular
 467 inverse grid in the readout space \mathcal{R} . To get an approximation of the inverse map
 468 in the entire readout space, we can use interpolation.

469 Since the inverse grid is irregular, trilinear interpolation cannot be applied.
 470 Given that the simulated map is dense enough to provide a good approxima-
 471 tion considering the size of our pads, we can adopt a similar approach (more
 472 complicated and computationally heavy alternative would be natural neighbor
 473 interpolation). As shown in Equation 1.12 in Section 1.1.2, trilinear interpolation
 474 can be expressed as a polynomial:

$$\hat{f}(x, y, z) = axyz + bxy + cxz + dyz + ex + fy + gz + h, \quad (3.14)$$

475 where a, b, c, d, e, f, g, h are coefficients uniquely determined by the values of
 476 the function at the vertices of the interpolation cell. We can generalize this
 477 for a function defined on an irregular grid. Given the function values at any eight
 478 points, we can write a system of eight linear equations

$$\begin{pmatrix} x_1 y_1 z_1 & x_1 y_1 & x_1 z_1 & y_1 z_1 & x_1 & y_1 & z_1 & 1 \\ \vdots & \vdots & \vdots & \vdots & \vdots & \vdots & \vdots & \vdots \\ x_8 y_8 z_8 & x_8 y_8 & x_8 z_8 & y_8 z_8 & x_8 & y_8 & z_8 & 1 \end{pmatrix} \begin{pmatrix} a \\ \vdots \\ h \end{pmatrix} = \begin{pmatrix} f(x_1, y_1, z_1) \\ \vdots \\ f(x_8, y_8, z_8) \end{pmatrix}, \quad (3.15)$$

479 which has a unique solution for the coefficients for most values of (x_n, y_n, z_n) and
 480 $f(x_n, y_n, z_n)$, where $n \in \{1, \dots, 8\}$.

481 This approach introduces a small complication: finding the correct pseudo-
 482 cell (i.e., the image of eight vertices forming a cubic cell in the regular grid) in
 483 the inverse grid. The eight irregularly spaced vertices of this pseudocell do not
 484 define a unique volume, so there are multiple possible ways to partition \mathcal{R} into
 485 pseudocells, with no obvious choice among them.

486 **We are currently ignoring this problem and performing binary search along**
 487 **x, y, z (in this order). It shouldn't matter too much because the 70/30 map**

488 doesn't cause such a big distortion and was even accidentally extrapolated for all
 489 z different from the central plane. Interpolation should be generally faster than
 490 the gradient descent since we don't need to iterate. We also don't need to optimize
 491 it to improve performance, if it's too slow we can even calculate the coefficients
 492 for the entire map before reconstruction.

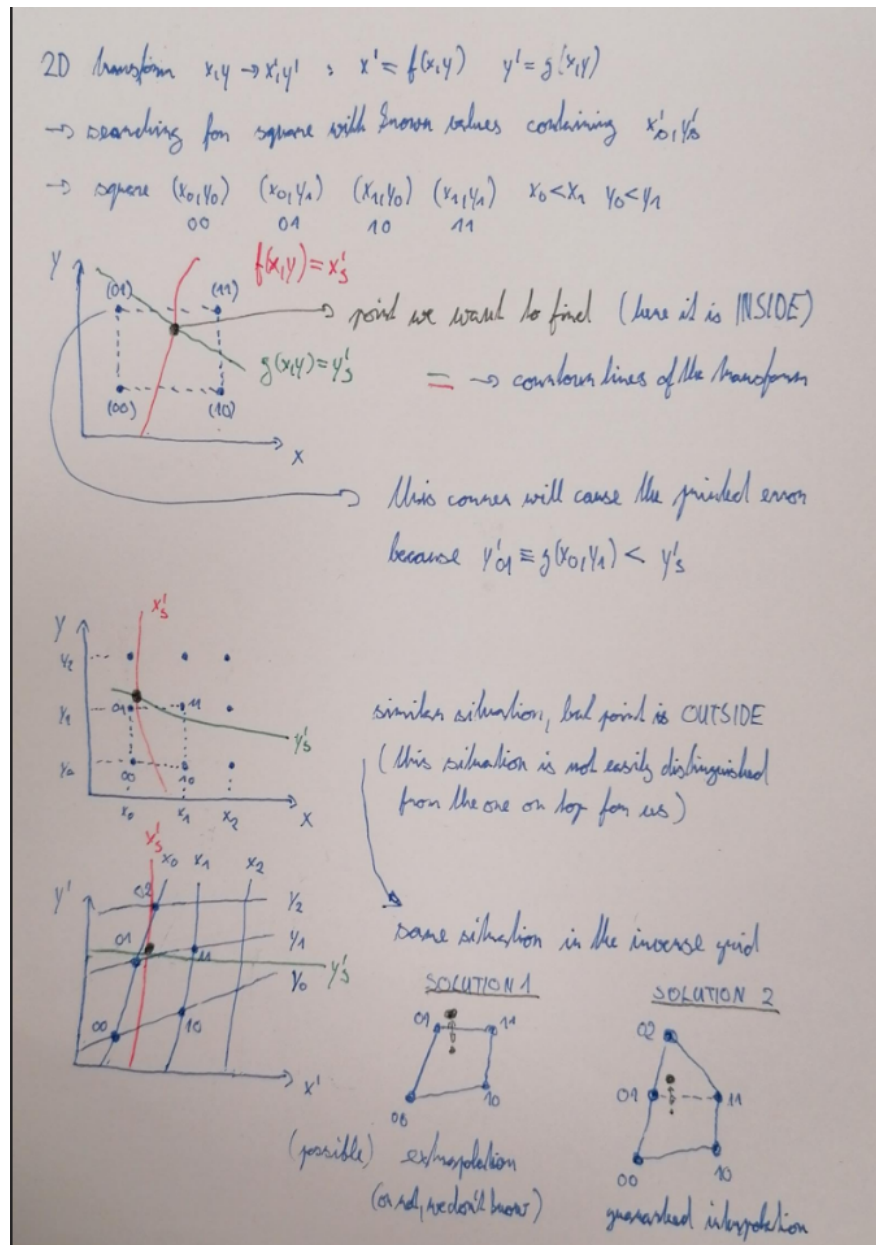


Figure 3.6: Selection of the points for interpolation. Create better images; use the explanation interpolation vs. extrapolation strange property. Solution 2 probably does not make much sense.

493 3.3 Discrete Reconstruction

494 Reconstruction with pads and time bins. Maybe testing different pads. Mapping
 495 the center of the pad (along with the midpoint of the time bin) isn't necessarily

496 the best approach since it might not correspond to the average parameters of
497 an electron with these readout parameters (insignificant?).

498 It is also possible to make this a subsection of the map, making the previous
499 subsections parts of a new subsection 'Map Inversion'.

4. Energy Reconstruction

The second stage is the reconstruction of the particle's energy using a fit of its reconstructed track (see Section 3). We have tested three ways of reconstructing the energy. Fitting is done using the MINUIT algorithm implemented in ROOT [2]. **Cite some CERN article directly on MINUIT, can add a section.**

The **Cubic Spline Fit** is a tested and later rejected method of energy reconstruction. It uses smoothly connected piecewise cubic polynomials between uniformly spaced nodes. Energy is calculated using the fit parameters by computing the radius of curvature in different points of the fitted curve using the known magnitude of the magnetic field perpendicular to the trajectory. We rejected this method because tuning of the fit to have a reasonably stable radius of curvature turned out to be unpractical.

The **Circle and Lines Fit** was chosen as an alternative since this corresponds to the shape of a trajectory of a charged particle crossing a finite volume with a homogeneous magnetic field. The energy of the particle can be estimated using the fitted radius and the magnitude of the perpendicular magnetic field in the middle of the TPC.

The **Runge-Kutta Fit** uses the 4th order Runge-Kutta numerical integration described in Section 2.2. Initial parameters of the track (including the particle's energy) are optimized so that the integrated trajectory fits to the reconstructed one. This fit can also be performed as a single parameter (i.e., energy) fit if we get the initial position and orientation of the particle on the entrance to the TPC from previous detectors (Tpx3 and MWPC, see Section 0.2).

4.1 Cubic Spline Fit

The first attempt to get an early estimate of the kinetic energy of the particle uses a cubic spline fit. We use an electron track starting in the origin of our coordinate system with an initial direction in the positive x axis. The example track is simulated microscopically (see Section 2.1) with a kinetic energy of 8 MeV in a gas mixture 90% Ar + 10% CO₂ (the same track was used in Section 3.1).

This track should probably be described in the simulation chapter.

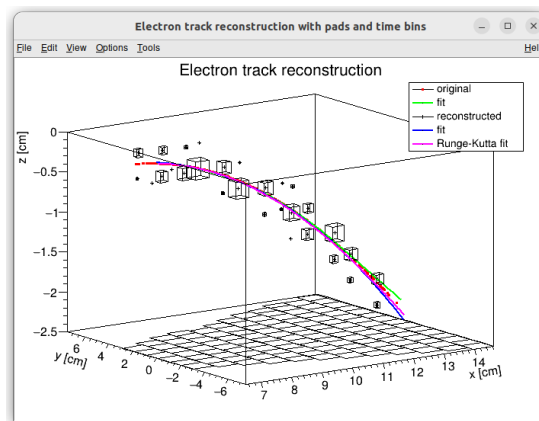


Figure 4.1: Example of a fitted reconstructed track. **Swap for better image.**

530 In order to calculate the spline, we use the class *TSpline3* from ROOT. This
 531 allows us to evaluate the spline using the coordinates (x_n, z_n) of each node and
 532 the derivatives d_1, d_2 in the first and the last node. We can fit these parameters
 533 of a fixed amount of nodes to the simulated trajectory. We use the IMPROVE
 534 algorithm provided by the *TMinuit* class in ROOT. This algorithm attempts to
 535 find a better local minimum after converging.

536 After the fit, we want to get an energy estimate. In order to calculate it, we
 537 need the radius of curvature, which we get from the fitted spline at every point
 538 of the trajectory. The part of the spline corresponding to a given node is defined
 539 as

$$z(x) = z_n + b\Delta x + c(\Delta x)^2 + d(\Delta x)^3, \quad (4.1)$$

540 where $\Delta x = x - x_n$ and b, c, d are coefficients. Using this equation, we derive
 541 the radius of curvature¹ as:

$$r(x) = \frac{(1 + z'^2(x))^{\frac{3}{2}}}{z''(x)} = \frac{(1 + (b + 2c\Delta x + 3d(\Delta x)^2)^2)^{\frac{3}{2}}}{2c + 6d\Delta x}. \quad (4.2)$$

542 Based on the geometry of the detector, we can assume the magnetic field
 543 $\mathbf{B}(x, 0, z) = (0, B(x, z), 0)$ for a track in the XZ plane. Since the electron is rela-
 544 tivistic, the effect of the electric field on its trajectory is negligible. The Lorentz
 545 force F_L is then always perpendicular to the momentum of the electron and acts
 546 as a centripetal force F_c :

$$\mathbf{F}_L = \mathbf{F}_c, \quad (4.3)$$

$$\|e\mathbf{v} \times \mathbf{B}\| = \frac{\gamma m_e v^2}{r}, \quad (4.4)$$

$$ec\beta B = \frac{E_{0e}\beta^2}{r\sqrt{1 - \beta^2}}, \quad (4.5)$$

$$\sqrt{1 - \beta^2} = \frac{E_{0e}\beta}{ecBr}, \quad (4.6)$$

547

$$\beta^2(x) = \left[1 + \left(\frac{E_{0e}}{ecB(x, z(x))r(x)} \right)^2 \right]^{-1}, \quad (4.7)$$

548 where e is the elementary charge, c is the speed of light in vacuum, m_e is the rest
 549 mass of electron, $E_{0e} = m_e c^2$ is the corresponding energy, γ is the Lorentz factor,
 550 \mathbf{v} is the velocity of the electron, and $\beta = \frac{v}{c}$. We can then finally get our estimate
 551 of the kinetic energy for a given point on the trajectory as follows:

$$E_{\text{kin}}(x) = \left(\frac{1}{\sqrt{1 - \beta^2(x)}} - 1 \right) E_{0e}. \quad (4.8)$$

552 We can then average these estimates at multiple points to get one final estimate.
 553 This method was later rejected in favor of the circle and lines fit described in
 554 Section 4.2. **Add some figures.**

¹For the general formula see https://en.wikipedia.org/wiki/Curvature#Graph_of_a_function

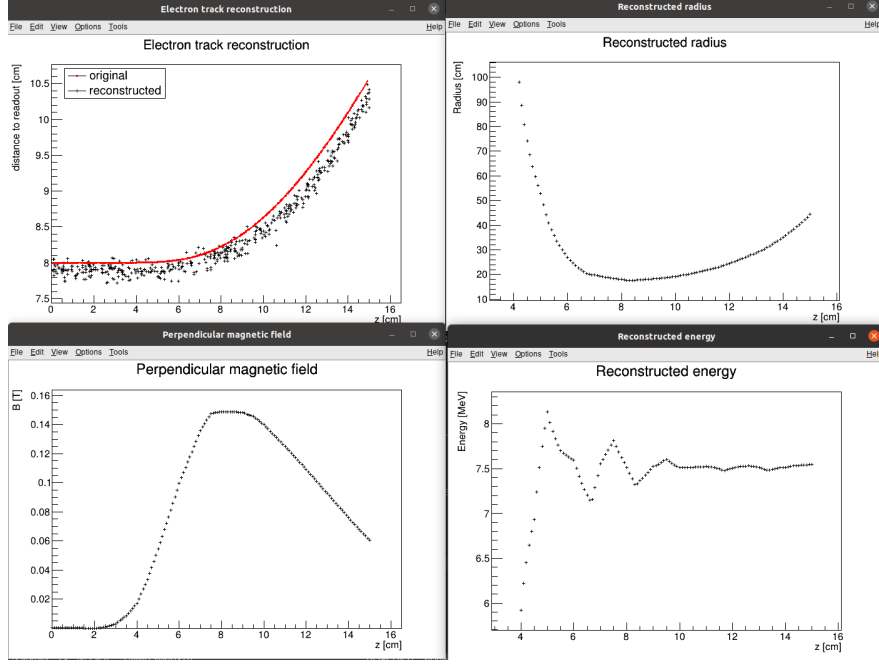


Figure 4.2: First attempt at a track reconstruction using only the drift velocity. Spline energy reconstruction attempt. **Swap for better image(s) – subfigure environment, correct coordinates.**

4.2 Circle and Lines Fit

Another way to estimate the particle’s kinetic energy is to fit its trajectory with a circular arc with lines attached smoothly. This shape of trajectory corresponds to a movement of a charged particle through a homogeneous magnetic field perpendicular to the particle’s momentum and limited to a certain volume. In general, the shape of such a trajectory in a non-perpendicularly oriented field is a spiral. In our case, this component is negligible since the field is approximately toroidal and the particle motion is nearly perpendicular to it. At first, we tested a 2D version of this fit, then we adapted it to 3D.

Our field is not homogeneous, it is therefore not entirely clear what value of magnetic field should be used along with the fitted radius (using equations 4.7 and 4.8) to get the best estimate for the kinetic energy. Since we only use this method as the first iteration of the particle’s energy that we later refine, an optimal solution of this problem is not required. Instead, we tested two options: taking the value of the field in the middle of the fitted circular arc and taking the average field along it. **We haven’t really tried to plot this for multiple tracks, but these estimates are saved somewhere and could be plotted.**

4.2.1 Two-dimensional fit

In the 2D case, the fitted function used for the electron track² described in Section 4.1 is defined as follows: **Maybe describe this track that we used at the beginning somewhere earlier (section microscopic simulations → Testing track?) so that it is easier to refer to it in multiple sections. It is not part of the early GitHub**

²Electron tracks bend towards negative z , we need to use the upper part of the circle

577 commits, so maybe it won't be possible to create exact replicas of the images,
578 but they should be at least very similar.

$$z(x) = \begin{cases} a_1x + b_1 & x < x_1 \\ z_0 + \sqrt{r^2 - (x - x_0)^2} & x_1 \leq x \leq x_2, \\ a_2x + b_2 & x > x_2 \end{cases} \quad (4.9)$$

579 where $a_{1,2}$ and $b_{1,2}$ are the parameters of the lines, (x_0, z_0) is the center of the cir-
580 cle, r is its radius, and $(x_{1,2}, z_{1,2})$ are the coordinates of the function's nodes.
581 That means we have 9 parameters ($z_{1,2}$ are not used in the function) along with
582 2 continuity conditions and 2 smoothness conditions. For the fit, we use the co-
583 ordinates of the nodes and the radius of the circle, which gives us 5 independent
584 parameters (only the radius has to be larger than half of the distance between
585 nodes). The continuity conditions (combined with the relations for $z_{1,2}$) are as
586 follows:

$$z_{1,2} = a_{1,2}x_{1,2} + b_{1,2} = z_0 - \sqrt{r^2 - (x_{1,2} - x_0)^2}. \quad (4.10)$$

587 The smoothness conditions are as follows:

$$a_{1,2} = \frac{x_0 - x_{1,2}}{\sqrt{r^2 - (x_{1,2} - x_0)^2}}. \quad (4.11)$$

588 Equation 4.10 gives us the values of $b_{1,2}$

$$b_{1,2} = z_{1,2} - a_{1,2}x_{1,2}. \quad (4.12)$$

589 For the coordinates of the center of the circle, we can use the fact that the center
590 has to lie on the axis of its chord. In other words, there is a value of a parameter t
591 such that, using the parametric equation of the axis

$$\begin{pmatrix} x_0 \\ z_0 \end{pmatrix} = \begin{pmatrix} \frac{x_1+x_2}{2} \\ \frac{z_1+z_2}{2} \end{pmatrix} + t \begin{pmatrix} \frac{z_2-z_1}{2} \\ \frac{x_1-x_2}{2} \end{pmatrix}. \quad (4.13)$$

592 At the same time, the center has to be in a distance of r from the nodes:

$$(x_1 - x_0)^2 + (z_1 - z_0)^2 = r^2, \quad (4.14)$$

$$\left(\frac{x_1 - x_2}{2} + \frac{z_1 - z_2}{2}t\right)^2 + \left(\frac{z_1 - z_2}{2} + \frac{x_2 - x_1}{2}t\right)^2 = r^2, \quad (4.15)$$

$$\left(\left(\frac{x_2 - x_1}{2}\right)^2 + \left(\frac{z_2 - z_1}{2}\right)^2\right)t^2 + \left(\frac{x_2 - x_1}{2}\right)^2 + \left(\frac{z_2 - z_1}{2}\right)^2 - r^2 = 0. \quad (4.16)$$

593 Since our electron track bends towards negative z and $x_2 > x_1$, we only care
594 about the solution with $t > 0$

$$t = \sqrt{\frac{r^2}{\left(\frac{x_2-x_1}{2}\right)^2 + \left(\frac{z_2-z_1}{2}\right)^2} - 1}, \quad (4.17)$$

595

$$x_0 = \frac{x_1 + x_2}{2} + \frac{z_2 - z_1}{2} \sqrt{\frac{r^2}{\left(\frac{x_2-x_1}{2}\right)^2 + \left(\frac{z_2-z_1}{2}\right)^2} - 1}, \quad (4.18)$$

$$z_0 = \frac{z_1 + z_2}{2} - \frac{x_2 - x_1}{2} \sqrt{\frac{r^2}{\left(\frac{x_2-x_1}{2}\right)^2 + \left(\frac{z_2-z_1}{2}\right)^2} - 1}. \quad (4.19)$$

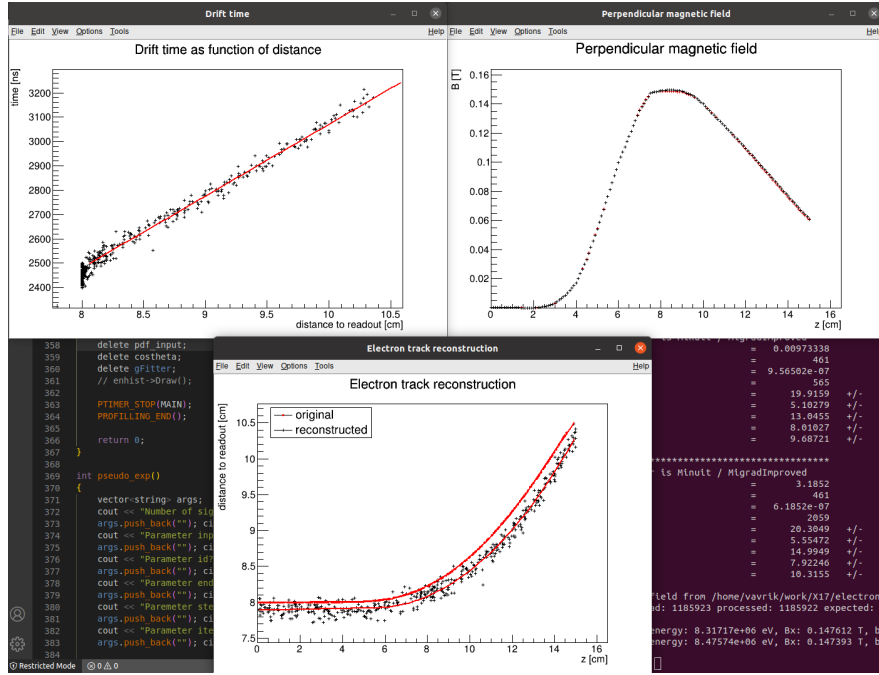


Figure 4.3: First attempt at a track reconstruction using only the drift velocity. Circle and Lines Fit in 2D. Swap for better image, correct coordinates.

The function defined in Equation 4.9 along with equations 4.11, 4.12, 4.18 and 4.19 derived using the continuity and smoothness conditions (combined with the relations for $z_{1,2}$) fully define our fitted function with parameters $r, x_{1,2}, z_{1,2}$. Some pictures of the fit on the tested track. Results of the fit. Again, the actual fit uses 8-z. Use GeoGebra schematics to generate a picture of 2D geometry.

Tested on a Runge-Kutta sample, and with microscopic tracks + map simulation. Preliminary 2D version (done) and complete 3D version. Geometry of the fit with its derivation.

4.2.2 Three-dimensional fit

Explain the geometry and least square method used for the 3D fit.

4.3 Runge-Kutta Fit

Single parameter fit with 4th order Runge-Kutta simulated track. Future testing with microscopic simulations and map simulation. Derivation of the geometry (least squares).

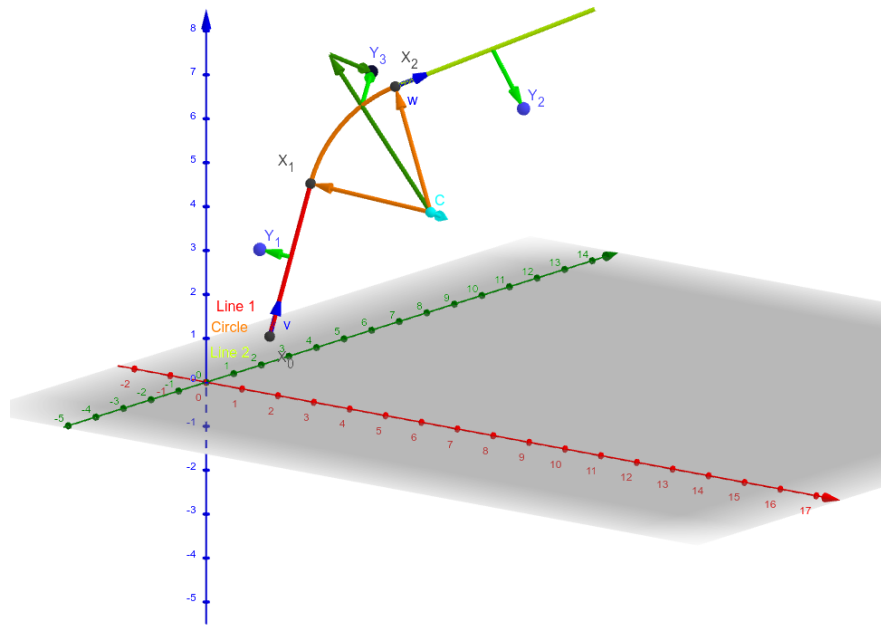


Figure 4.4: Circle and Lines Fit 3D geometry. [Swap for better image.](#)

Conclusion

Here or at the end of each section. Something about the future of this work?

Notes

General notes about the thesis:

- Check that all of the classes and other code are marked the same way in the text. I used italics somewhere, could use different font for this instead.
- Check unbreakable space in front of articles. Remove excessive article usage with proper nouns.
- Currently using margins for single-sided printing (bigger on the left side).
- Check that present tense is used
- American English quotation marks (") instead of British English (').
- Some of the overfull hbox warnings might change if duplex printing is used (they generate black rectangles on the edge of the page), leaving them be for now
- Check nobreakdash usage
- Check capitalized references (e.g., Figure, Section, Equation)
- Check $\langle \dots \rangle$ math mode instead of $\$ \dots \$$. (actually unlike $\langle \dots \rangle$ math mode, there is apparently no real benefit to this clumsy syntax)
- Use siunitx package to ensure correct formatting.
- Check other stuff that's written in the MFF UK template.

Random notes:

- Only electrons that start and end in the sector closer than 0.5 cm are used for reconstruction (newest version).

Future

Things planned for the future:

- Testing the reconstruction algorithm by measuring real particles with a known energy distribution.
- The **Fast Simulation with Ionization Electron Map** is planned for the future. It will use the HEED program [24] to simulate the primary particle and the Ionization Electron Map (see Section 3.2) to simulate the drift of secondary electrons. It should be significantly faster than the Microscopic Simulation but offer comparable precision since it will rely on an already simulated drift map. (Primary track simulated in HEED. Readout parameters by interpolating the map. Diffusion from the map for randomization.)

- Account for GEM, delta electrons, ...
- Likelihood approach instead of least squares (if it improves the reconstruction significantly), we should at least use a better method than taking the center of the TPC bin.
- More detailed electric field simulation (if needed, GEM will have more complex field)

Likelihood - inverse map

If we wanted to further improve this procedure, taking into account the whole map \mathcal{M} , we could make an "inverse map" from \mathcal{R} to distributions on \mathcal{D} . We could achieve this by taking the normalized probability density of an electron with initial coordinates (x, y, z) having readout coordinates (x', y', t) . If we fix (x', y', t) , we get an unnormalized probability density $f(x, y, z) = \mathcal{M}_{(x, y, z)}(x', y', t)$ (assuming that all initial coordinates are a priori equally likely). This could potentially improve the discrete reconstruction if we take the mean value of this probability density across the pad and time bin

$$f_{\text{pad, bin}}(x, y, z) = \frac{1}{A_{\text{pad}} \Delta t_{\text{bin}}} \int_{\text{pad, bin}} \mathcal{M}_{(x, y, z)}(x', y', t) dx' dy' dt \quad (4.20)$$

and using it for a likelihood fit instead of using least squares. This still assumes that all initial coordinates are equally likely which is clearly not the case for a primary particle track. In the future, we could even use the fast track simulation with the map (should be possible to make around 1000 tracks per minute per core with current settings), create a big set of tracks with reasonable parameters and use these to get an approximation of the probability distribution of the detector response. Some approximations would be necessary when interpreting the data to decrease the degrees of freedom of this distribution (we would have to pick a set of parameters and assume that some of them are independent). This could give us an idea about the best achievable resolution (how significantly will the detector response differ for a given change in energy). If the difference is significant, we could try to further improve the likelihood fit.

Bibliography

- [1] Garfield++. <https://garfieldpp.web.cern.ch/garfieldpp/>. Accessed: 2023-05-18.
- [2] Rene Brun and Fons Rademakers. Root — An Object Oriented Data Analysis Framework. *Nuclear Instruments and Methods in Physics Research Section A: Accelerators, Spectrometers, Detectors and Associated Equipment*, 389(1–2):81–86, Apr 1997. Proceedings AIHENP’96 Workshop, Lausanne, Sep. 1996, See also <https://root.cern/>, Paper published in the Linux Journal, Issue 51, July 1998.
- [3] About MetaCentrum. <https://metavo.metacentrum.cz/en/about/index.html>, 2023. Accessed: 2024-11-27.
- [4] M. E. Rose. Internal Pair Formation. *Phys. Rev.*, 76:678–681, Sep 1949.
- [5] R. Essig, J. A. Jaros, W. Wester, P. Hansson Adrian, S. Andreas, T. Averett, O. Baker, B. Batell, M. Battaglieri, J. Beacham, T. Beranek, J. D. Bjorken, F. Bossi, J. R. Boyce, G. D. Cates, A. Celentano, A. S. Chou, R. Cowan, F. Curciarello, H. Davoudiasl, P. deNiverville, R. De Vita, A. Denig, R. Dharmapalan, B. Dongwi, B. Döbrich, B. Echenard, D. Espriu, S. Fegan, P. Fisher, G. B. Franklin, A. Gasparian, Y. Gershtein, M. Graham, P. W. Graham, A. Haas, A. Hatzikoutelis, M. Holtrop, I. Irastorza, E. Izaguirre, J. Jaeckel, Y. Kahn, N. Kalantarians, M. Kohl, G. Krnjaic, V. Kubarovsky, H-S. Lee, A. Lindner, A. Lobanov, W. J. Marciano, D. J. E. Marsh, T. Maruyama, D. McKeen, H. Merkel, K. Moffeit, P. Monaghan, G. Mueller, T. K. Nelson, G. R. Neil, M. Oriunno, Z. Pavlovic, S. K. Phillips, M. J. Pivovarov, R. Poltis, M. Pospelov, S. Rajendran, J. Redondo, A. Ringwald, A. Ritz, J. Ruz, K. Saenboonruang, P. Schuster, M. Shinn, T. R. Slatyer, J. H. Steffen, S. Stepanyan, D. B. Tanner, J. Thaler, M. E. Tobar, N. Toro, A. Upadye, R. Van de Water, B. Vlahovic, J. K. Vogel, D. Walker, A. Weltman, B. Wojtsekhowski, S. Zhang, and K. Zioutas. Dark Sectors and New, Light, Weakly-Coupled Particles, 2013.
- [6] F.W.N. de Boer, O. Fröhlich, K.E. Stiebing, K. Bethge, H. Bokemeyer, A. Balanda, A. Buda, R. van Dantzig, Th.W. Elze, H. Folger, J. van Klinken, K.A. Müller, K. Stelzer, P. Thee, and M. Waldschmidt. A deviation in internal pair conversion. *Physics Letters B*, 388(2):235–240, 1996.
- [7] F W N de Boer, R van Dantzig, J van Klinken, K Bethge, H Bokemeyer, A Buda, K A Müller, and K E Stiebing. Excess in nuclear pairs near 9 MeV/ invariant mass. *Journal of Physics G: Nuclear and Particle Physics*, 23(11):L85, nov 1997.
- [8] F W N de Boer, K Bethge, H Bokemeyer, R van Dantzig, J van Klinken, V Mironov, K A Müller, and K E Stiebing. Further search for a neutral boson with a mass around 9 MeV/c². *Journal of Physics G: Nuclear and Particle Physics*, 27(4):L29, apr 2001.

- [9] Attila Vitéz, A. Krasznahorkay, J. Gulyas, Margit Csátos, Lorant Csige, Zoltan Gacsi, Barna Nyakó, F. Boer, T. Ketel, and J. Klinken. Anomalous Internal Pair Creation in ^8Be as a Signature of the Decay of a New Particle. *Acta Physica Polonica B - ACTA PHYS POL B*, 39:483, 02 2008.
- [10] A. Krasznahorkay, J. Gulyas, Margit Csátos, Attila Vitéz, T. Tornyai, L. Stuhl, Lorant Csige, Zoltan Gacsi, A. J. Krasznahorkay, M. Hunyadi, and T.J. Ketel. Searching for a light neutral axial-vector boson in isoscalar nuclear transitions. *Frascati Physics Series*, 56:86, 10 2012.
- [11] A. J. Krasznahorkay, M. Csátlós, L. Csige, Z. Gácsi, J. Gulyás, M. Hunyadi, I. Kuti, B. M. Nyakó, L. Stuhl, J. Timár, T. G. Tornyai, Zs. Vajta, T. J. Ketel, and A. Krasznahorkay. Observation of Anomalous Internal Pair Creation in ^8Be : A Possible Indication of a Light, Neutral Boson. *Physical Review Letters*, 116(4), January 2016.
- [12] D.R. Tilley, J.H. Kelley, J.L. Godwin, D.J. Millener, J.E. Purcell, C.G. Sheu, and H.R. Weller. Energy levels of light nuclei $A=8,9,10$. *Nuclear Physics A*, 745(3):155–362, 2004.
- [13] N. J. Sas, A. J. Krasznahorkay, M. Csátlós, J. Gulyás, B. Kertész, A. Krasznahorkay, J. Molnár, I. Rajta, J. Timár, I. Vajda, and M. N. Harakeh. Observation of the X17 anomaly in the $^7\text{Li}(p,e^+e^-)^8\text{Be}$ direct proton-capture reaction, 2022.
- [14] A. J. Krasznahorkay, M. Csátlós, L. Csige, J. Gulyás, A. Krasznahorkay, B. M. Nyakó, I. Rajta, J. Timár, I. Vajda, and N. J. Sas. New anomaly observed in ^4He supports the existence of the hypothetical X17 particle. *Physical Review C*, 104(4), October 2021.
- [15] D.R. Tilley, H.R. Weller, and G.M. Hale. Energy levels of light nuclei $A = 4$. *Nuclear Physics A*, 541(1):1–104, 1992.
- [16] A. J. Krasznahorkay, A. Krasznahorkay, M. Begala, M. Csátlós, L. Csige, J. Gulyás, A. Krakó, J. Timár, I. Rajta, I. Vajda, and N. J. Sas. New anomaly observed in ^{12}C supports the existence and the vector character of the hypothetical X17 boson. *Phys. Rev. C*, 106:L061601, Dec 2022.
- [17] F. Ajzenberg-Selove. Energy levels of light nuclei $A = 11,12$. *Nuclear Physics A*, 506(1):1–158, 1990.
- [18] Péter Kálmán and Tamás Keszthelyi. Anomalous internal pair creation. *The European Physical Journal A*, 56, 08 2020.
- [19] A. Aleksejevs, S. Barkanova, Yu. G. Kolomensky, and B. Sheff. A Standard Model Explanation for the "ATOMKI Anomaly", 2021.
- [20] Jonathan L. Feng, Bartosz Fornal, Iftah Galon, Susan Gardner, Jordan Smolinsky, Tim M. P. Tait, and Philip Tanedo. Protophobic Fifth-Force Interpretation of the Observed Anomaly in ^8Be Nuclear Transitions. *Phys. Rev. Lett.*, 117:071803, Aug 2016.

- [21] Tran The Anh, Tran Dinh Trong, Attila J. Krasznahorkay, Attila Krasznahorkay, József Molnár, Zoltán Pintye, Nguyen Ai Viet, Nguyen The Nghia, Do Thi Khanh Linh, Bui Thi Hoa, Le Xuan Chung, and Nguyen Tuan Anh. Checking the 8Be Anomaly with a Two-Arm Electron Positron Pair Spectrometer. *Universe*, 10(4):168, April 2024.
- [22] Kh. U. Abraamyan, Ch. Austin, M. I. Baznat, K. K. Gudima, M. A. Kozhin, S. G. Reznikov, and A. S. Sorin. Observation of structures at ~ 17 and ~ 38 MeV/c² in the $\gamma\gamma$ invariant mass spectra in pC, dC, and dCu collisions at p_{lab} of a few GeV/c per nucleon, 2023.
- [23] The MEG II collaboration, K. Afanaciev, A. M. Baldini, S. Ban, H. Benmansour, G. Boca, P. W. Cattaneo, G. Cavoto, F. Cei, M. Chiappini, A. Corvaglia, G. Dal Maso, A. De Bari, M. De Gerone, L. Ferrari Barusso, M. Francesconi, L. Galli, G. Gallucci, F. Gatti, L. Gerritzen, F. Grancagnolo, E. G. Grandoni, M. Grassi, D. N. Grigoriev, M. Hildebrandt, F. Ignatov, F. Ikeda, T. Iwamoto, S. Karpov, P. R. Kettle, N. Khomutov, A. Kolesnikov, N. Kravchuk, V. Krylov, N. Kuchinskiy, F. Leonetti, W. Li, V. Malyshev, A. Matsushita, M. Meucci, S. Mihara, W. Molzon, T. Mori, D. Nicolò, H. Nishiguchi, A. Ochi, W. Ootani, A. Oya, D. Palo, M. Panareo, A. Papa, V. Pettinacci, A. Popov, F. Renga, S. Ritt, M. Rossella, A. Rozhdestvensky, S. Scarpellini, P. Schwendimann, G. Signorelli, M. Takahashi, Y. Uchiyama, A. Venturini, B. Vitali, C. Voena, K. Yamamoto, R. Yokota, and T. Yonemoto. Search for the X17 particle in ${}^7\text{Li}(p, e^+e^-){}^8\text{Be}$ processes with the MEG II detector, 2024.
- [24] I.B. Smirnov. Modeling of ionization produced by fast charged particles in gases. *Nuclear Instruments and Methods in Physics Research Section A: Accelerators, Spectrometers, Detectors and Associated Equipment*, 554(1):474–493, 2005.
- Acknowledgments:** Computational resources were provided by the e-INFRA CZ project (ID:90254), supported by the Ministry of Education, Youth and Sports of the Czech Republic.

List of Figures

| | | | |
|-----|-----|---|----|
| 782 | | | |
| 783 | 1 | The ATOMKI anomalous IPC measured for different nuclei. . . . | 4 |
| 784 | 2 | Results from the Hanoi spectrometer – angular e^+e^- pair correlations measured in the ${}^7\text{Li}(p, e^+e^-){}^8\text{Be}$ reaction at $E_p = 1225$ keV [21]. | 5 |
| 785 | | | |
| 786 | 3 | Results from the MEG II experiments – angular correlation of e^+e^- pairs with $E_{\text{sum}} \in [16, 20]$ MeV measured in the ${}^7\text{Li}(p, e^+e^-){}^8\text{Be}$ reaction with proton beam energies 500 and 1080 keV. The 500 keV dataset is fitted with Monte Carlo of both the IPC deexcitation and the EPC produced by gammas [23]. | 6 |
| 787 | | | |
| 788 | | | |
| 789 | | | |
| 790 | | | |
| 791 | 1.1 | Pad layout of the TPC. Swap for better image. | 8 |
| 792 | 1.2 | Visualization of trilinear interpolation as a composition of linear interpolations. Image drawn in GeoGebra and inspired by a similar image on Wikipedia (which looks a bit worse) – is credit necessary? | 10 |
| 793 | | | |
| 794 | | | |
| 795 | 2.1 | Example of a simulated electron track in 70 % argon and 30 % CO_2 atmosphere (on the left). Swap for better images, better zoom. Explain drift lines, primary particle. | 12 |
| 796 | | | |
| 797 | | | |
| 798 | 2.2 | Comparison of diffusion in a simulated electron track in 70 % argon, 30 % CO_2 atmosphere and in 90 % argon, 10 % CO_2 atmosphere (on the right). Swap for better image, better zoom. Or put the same pictures for both comparisons in one subfigure, etc. Describe better. | 12 |
| 799 | | | |
| 800 | | | |
| 801 | | | |
| 802 | | | |
| 803 | 3.1 | Dependence of the drift time on the z coordinate in 90 % argon and 10 % CO_2 atmosphere, fitted with a linear function. The fitted function gives us the average drift velocity in the gas and can be used for rough reconstruction in our TPC. Swap for better image with axis labels, etc. Maybe write the fitted equation. | 14 |
| 804 | | | |
| 805 | | | |
| 806 | | | |
| 807 | | | |
| 808 | 3.2 | First attempt at a track reconstruction using only the drift velocity. This approach works well in a standard TPC (ideally cite some source?). 90 % argon and 10 % CO_2 atmosphere. Swap for better image, correct coordinates. | 15 |
| 809 | | | |
| 810 | | | |
| 811 | | | |
| 812 | 3.3 | First attempt at a track reconstruction using only the drift velocity, residues. Swap for better image, correct coordinates. What's causing the shift? Explain details. | 15 |
| 813 | | | |
| 814 | | | |
| 815 | 3.4 | Example of map generation. Swap for better image, correct coordinates. | 17 |
| 816 | | | |
| 817 | 3.5 | Example reconstruction with the map. Swap for better image, correct coordinates. | 18 |
| 818 | | | |
| 819 | 3.6 | Selection of the points for interpolation. Create better images; use the explanation interpolation vs. extrapolation strange property. Solution 2 probably does not make much sense. | 20 |
| 820 | | | |
| 821 | | | |
| 822 | 4.1 | Example of a fitted reconstructed track. Swap for better image. . | 22 |
| 823 | 4.2 | First attempt at a track reconstruction using only the drift velocity. Spline energy reconstruction attempt. Swap for better image(s) – subfigure environment, correct coordinates. | 24 |
| 824 | | | |
| 825 | | | |

| | | | |
|-----|-----|--|----|
| 826 | 4.3 | First attempt at a track reconstruction using only the drift velocity. Circle and Lines Fit in 2D. Swap for better image, correct coordinates. | 26 |
| 827 | | | |
| 828 | | | |
| 829 | 4.4 | Circle and Lines Fit 3D geometry. Swap for better image. | 27 |

830 List of Tables

831 List of Abbreviations

832 **GEM** Gas Electron Multiplier

833 **HEED** High Energy Electro-Dynamics

834 **IEAP CTU** Institute of Experimental and Applied Physics, Czech Technical
835 University in Prague

836 **IPC** Internal Pair Creation

837 **EPC** External Pair Creation

838 **MWPC** Multi-Wire Proportional Chamber

839 **OFTPC** Orthogonal Fields TPC

840 **TPC** Time Projection Chamber

841 **ToA** time-of-arrival

842 **ToT** time-over-threshold

843 **Tpx3** Timepix 3